REVISION 2

1   The topological model for defects and interfaces in complex crystal structures

2   J.P. Hirth[1], Jian Wang[2], and Greg Hirth[3*]

3   [1]Emeritus Professor, Ohio State and Washington State Universities, 546 S. Park Centre Ave.,

4   Green Valley, AZ 54614. USA

5   [2]Mechanical and Materials Engineering Department, University of Nebraska-Lincoln, Lincoln,

6   NE68588. USA

7   [3]Department of Geological Sciences, Brown University, Providence RI 02912. USA

8   * Corresponding author, Greg_Hirth@brown.edu

9   Key words: twinning; mineral; structural group; dislocations; disconnections; topological model

10   **Abstract**

11   The topological model (TM) is presented for the complex crystal structures characteristic of

12   some minerals. We introduce a tractable method for applying the TM to characterize defects in

13   these complex materials. Specifically, we illustrate how structural groups, each with a motif

14   containing multiple atoms, provide lattices and structures that are useful in describing

15   dislocations and disconnections in interfaces. Simplified methods for determining the shuffles

16   that accompany disconnection motion are also described. We illustrate the model for twinning in

17   albite owing to its potential application for constraining the rheological properties of the crust at

18   conditions near the brittle-plastic transition, where plagioclase is a major constituent of common

19   rock types. While deformation twins in plagioclase are often observed in crustal rocks, the

20   interpretation of the stress states at which they form has not advanced. The concept of structural

21   groups makes analysis of the twinning process easier in complex minerals and explicitly predicts

22   the interface structure of the deformation twins.

REVISION 2

23 **1. Introduction**

24   The topological theory, based on crystal symmetry with added symmetry elements at

25 interfaces (Pond and Vachavas, 1983), was developed to describe interfaces and defects in

26 crystals (Pond, 1989). It was expanded to include a formal description of defects called

27 disconnections (Hirth and Pond, 1996). The topological model (TM), entails the application of

28 these ideas to describe dislocations and disconnections at interfaces, including those that provide

29 the mechanism for growth of a phase normal to the interface (Pond et al, 2007). The same

30 defects account for interface structure and misfit accommodation. While almost all applications

31 have dealt with simple metals and simple compounds (e.g., Medlin and Yang, 2010), the TM has

32 many potential applications in earth and planetary sciences, for a wide range of minerals.

33 However, there are added factors that must be considered for more complicated minerals (i.e.,

34 with low symmetry and/or a large number of atoms in the unit cell) such as the plagioclase

35 feldspars. Here, we review the topological model and then introduce new concepts useful in the

36 application of the TM to more complicated mineral structures.

37   Disconnections are linear interface defects with both a step character and dislocation

38 components characterized by the Burgers vector. Motion of the disconnection can be envisioned

39 to occur by a simple engineering shear associated with motion of the dislocation part, and local

40 rearrangements of atoms (shuffles) associated with motion of the step part. These components of

41 the TM and a view of a disconnection are illustrated in Appendix A for the case of a twin in a

42 simple cubic structure. In metals, step heights are small and shuffles are either absent or simple.

43 Minerals often have complex structures containing many atoms, so step heights and

44 corresponding Burgers vectors can be large and the associated shuffles are numerous. To

45 facilitate application of the TM to these complex mineral structures, we propose the concept of a

REVISION 2

46   lattice of structural groups, and show that this yields the Burgers vector in the TM description.

47   While these ideas are general, and can be extended to other processes such as phase

48   transformations and grain boundary sliding (as outlined in the discussion), we introduce these

49   concepts for twinning, using the example of low albite.

50   Defect properties can be determined by circuit mapping (*e.g.,* the familiar Burgers circuits for

51   dislocations) or by line integrals of symmetry elements. These two techniques were compared in

52   Pond and Hirth (1994) and shown to give equivalent results for defects in twinning and phase

53   transformations, where translation and rotation are the principal symmetry elements. For

54   complex crystal structures, the new concept of a lattice of structural groups makes the circuit

55   mapping technique significantly more tractable. Our focus is on disconnections, interface defects

56   that provide the mechanism for shear-type phase transformation and twinning (reviewed in Hirth

57   et al., 2013; 2016) and grain boundary processes (reviewed in Han et al., 2018). More general

58   symmetry considerations and other types of defects are treated in Pond (1989).

59   **2. Reference spaces**

60   As reviewed in Howe et al (2009), early work indicated that transformation defects have step

61   character. Building on the early work, the TM precisely defined the Burgers vector and step

62   height of a disconnection in reference spaces. In sections 2.1 – 2.3, we describe three perfect

63   reference spaces in the TM, analogous to reference structures for the familiar Burgers circuits for

64   dislocations (Anderson et al., 2018). The volume transformed when the disconnection moves by

65   one repeat distance defines an exchange cell (e-cell) that contains all displacements associated

66   with the transformation.

67

REVISION 2

68   **2.1 The Coherent Dichromatic Pattern**

69   The fundamental crystal structure of interfaces is a dichromatic arrangement that superposes

70   the lattices of the two crystals on either side of the interface; by convention, we refer to these as

71   the matrix μ and product λ lattices (Figure A1b). The first reference space is the coherent

72   dichromatic pattern (CDP), which is the superposition of the Bravais lattices of the two crystals.

73   A perfect twin boundary is naturally coherent, but we retain the coherent modifier to emphasize

74   that the same reference applies to facets on twin boundaries and to phase transformations, where

75   coherency stresses are present at the interface. The origin of the CDP is at a maximum

76   symmetry, coincident lattice point on a coincident site plane, e.g., the twin plane. In detail, the

77   CDP is more general than the coincidence site lattice in that there is no need for registry in the

78   direction normal to the interface. The symmetry of the CDP is the union of that of the two

79   component crystals extended by an anti-symmetry element (designated with a prime ') unique to

80   the pattern (Pond, 1989). In the resulting dichromatic space group, some of the point symmetry

81   elements are coincident and some are anti-symmetric. For an example of the latter, all perfect

82   twins have m' mirror symmetry. A number of examples of CDPs in simple metals are given in

83   Hirth et al (2013). In contrast, numerous minerals have unit cells containing many atoms. In the

84   following we show paired reference spaces in CDPs for a simple cubic lattice and for the

85   example of a twin in low albite.

86   The composition of low albite is ($NaAlSi_3O_8$) and its conventional unit cell is shown in Fig.

87   1. The lattice parameters are $a = 0.814\ nm, b = 1.2785\ nm$ and $c = 0.7158\ nm$. The

88   triclinic angles are $\alpha = 94.2°, \beta = 116.6°$, and $\gamma = 87.7°$. The crystal structure entails a C_i

89   point group and a $C1 - P\bar{1}$ space group, triclinic with a center of inversion and a basis of four,

90   with indices (*hkl*). As discussed in Hahn (2014), Wenk and Bulakh (2016), Ribbe (1974), this is

REVISION 2

91   a large unit cell selected to parallel the $C1$ monoclinic structure of orthoclase. An alternate

92   (smaller) $C1$ unit cell is shown in red in Fig. 2, with indices $(hkl)^0$. The lattice parameters are

93     $a^0 = 0.814\ nm$, $b^0 = 0.7716\ nm$ and $c^0 = 0.7158\ nm$. The triclinic angles are $\alpha =$

94   107.27^o, $\beta = 116.61^o$, and $\gamma = 55.87^o$. From a defect viewpoint, the vectors in the small cell

95   represent possible perfect Burgers vectors. For example, when considering Burgers vectors in

96   plagioclase (e.g., Stünitz et al (2003) using the larger conventional cell, the vectors ½ [110] and

97   ½[1$\bar{1}$0] are perfect Burgers vectors (i.e., [010] and [0$\bar{1}$0]) when using the smaller cell (Figure 2).

98   The CDP for albite is shown in Fig. 3. Translation vectors $\mathbf{t}_\mu$ and $\mathbf{t}_\lambda$, with a common origin,

99   connect lattice sites. For twinning and many phase transformations, the circuits in the topological

100   theory reduce to the limiting form of the translation vectors in the two lattices (Pond, 1989).

101   Then the Burgers vectors $\mathbf{b}$ for dislocation components of disconnections or for interface

102   dislocations are given by

103                  $$\mathbf{b} = \mathbf{t}(\lambda) - \mathbf{t}(\mu) \tag{1}$$

104   Disconnections comprise a dislocation component $\boldsymbol{b}$ and a step component with height h. In

105   general, the height is given by

106                  $$h = ih_0 \tag{2}$$

107   where i is an integer and h_0 is equal to the interplanar spacing d of twin (or terrace) planes.

108   Figure 4 shows how a disconnection could be formed from crystals with free surfaces containing

109   steps. The step height of the disconnection is the smaller of h_λ and h_μ. Disconnections separate

110   low-index terraces and their motion provides the mechanism for growth normal to the terraces.

111   The specific disconnection properties are selected so that the structure of the terraces on either

112   side of the defect are identical. The Burgers vector and step height for a specific disconnection

REVISION 2

113   with $h = h_0$ are included in Fig. 4. Thus, some disconnection properties, **b** and h, are directly

114   determinable from the CDP.

115

2.2 The Coherent Dichromatic Complex

117   The second reference structure is the coherent dichromatic complex (CDC). The CDC is the

118   superposition of the μ and λ crystal structures and includes the local atomic motif (formally the

119   point group) at a lattice site. Thus, the CDC is a space group that often has lower symmetry than

120   the CDP. The total displacements, $\mathbf{u}(\lambda)$ and $\mathbf{u}(\mu)$, accompanying twinning are depicted in the

121   CDC. The displacement of a given atom is the sum of the shear displacement associated with the

122   dislocation component and the local shuffle displacement that completes the transformation. A

123   simple example of shuffles is shown in Fig. A1. In most cases the CDC has coincident symmetry

124   and we write the displacements as $\mathbf{u}^0(\lambda)$ and $\mathbf{u}^0(\mu)$. In some cases, the two structures

125   comprising the CDC can be offset uniformly by a vector **p** as a consequence of interfacial free

126   energy minimization, with the consequences discussed in Appendix A. Both the μ and λ atoms

127   are displaced by **p** in the e-cell, so the portion of the shuffles associated with **p** cancels. For this

128   reason and because **p** is rarely measured and, when present, is often very small, we neglect it

129   here, so that $\mathbf{u}^0(\mu) = 0$. Then, the shuffles of a given atom are determined by analysis of $\Delta\mathbf{u}$ in

130   the CDC, and are given by:

131    $$\mathbf{s} = \mathbf{u}^0(\lambda) - \mathbf{u}^0(\mu) - \mathbf{b} = \mathbf{u}^0(\lambda) - \mathbf{b} \ . \tag{3}$$

132   Alternatively, a shifted dichromatic complex (SDC), where **b** is subtracted from $\mathbf{u}^0(\lambda)$

133   (Appendix A and Fig. A1c) is useful in describing shuffles. The displacements of a given atom in

REVISION 2

134 the SDC are those associated only with the shuffles, $\mathbf{u}(\lambda) = \boldsymbol{u}^0(\lambda) - \mathbf{b}$. Hence, the same

135 shuffles are given by

$$\mathbf{s} = \mathbf{u}(\lambda) \qquad\qquad (4)$$

136 Similarly, if the two lattices rotate as a consequence of transformation, the Burgers vectors and

137 shuffles are represented in a rotated RCDP or RDC, respectively (Hirth et al., 2013).

138   Here we illustrate how the concept of structural groups facilitates the characterization of

139 defects. A unit cell comprised of structural group dipoles is shown in Fig. 5a. The motifs of a

140 structural group dipole in the atomic CDC are depicted in Fig 5b. Figure 5c is a rotated view of

141 the motifs with the twinning direction pointing toward the viewer. The unit cell shown in Fig. 5a

142 comprises structural group dipoles centered on cell corners. In both Fig. 5a and 5b, the dipoles

143 represent the matrix part of the e-cell: the smallest repeating unit of transformation. As seen in

144 Figure 5b, all atoms occur in pairs with their midpoints at the center of the pair at the same

145 position as the center of the structural group dipole. Hence, the atom pairs also exhibit inversion

146 symmetry. The cell of structural groups is triclinic P$\bar{1}$ with a basis of two. A portion of the CDC

147 is presented in Fig. 6. To maintain twin symmetry, the structural group dipoles are displaced in

148 the [010] direction, producing a rotation. The rotation can be represented by a vector $\mathbf{R} = \mathbf{n}\theta$,

149 where $\mathbf{n}$ is a unit vector along the axis of rotation, perpendicular to the line connecting the dipole

150 members, and θ is the angle of rotation in the plane normal to $\mathbf{n}$. For lower albite, $\mathbf{n}$= [-0.0432 0

151 1] and $\theta = 8.4$ degrees. Fig. 6a shows that the component of $\mathbf{R}$ normal to (010) is zero as a

152 structural group moves from the matrix to the twin. However, the out-of-plane rotation is non-

153 zero (Fig. 6b). The $\mathbf{R}$ vector lies in the (010) plane, with components $(R_1, 0, R_3)$. Hence, for the

154 $h = 1$ albite twin, all shuffles are associated with this rotation, *i.e.*, the entire unit in Fig. 6a

REVISION 2

155   rotates during the twin transformation. The use of structural groups simplifies the analysis of

156   shuffles, which otherwise would be difficult.

157   We split the shuffle analysis for albite into several stages. The CDC for structural groups is

158   shown in Figure 6. A depiction of the full CDC would be too complicated, so we show the

159   matrix and the twin separately and deduce the CDC or SDC from these figures. Figures 7a, 7b,

160   and 7c show the matrix, a portion of the matrix sheared but not shuffled, and the true twin,

161   respectively. All are projected along $-\boldsymbol{\eta}$, which is very close to $[201]^0 = [201]$. Here, **b** has

162   an out-of-plane component, which is already known from the CDP. One can imagine the SDP by

163   extending the lattices in Fig. 7b and deducing the displacements that create the true twin shown

164   in Fig. 7c. In the creation of the true twin, the net result of the shuffles is to rotate the motif

165   dipole in Fig. 5b by the same angle θ as the structural groups in Fig. 5a. This accomplishes one

166   increment of transformation. The shuffles are of two types, exchanges, and shifts. The exchange-

167   type shuffles are apparent in the SDC of Fig. 7c, or, less straightforwardly, from the CDC of Fig.

168   7b. For the SDC the final structure after shuffling is equivalent to the rotation of the dipole

169   illustrated in Fig. 5a about **n** by the same angle as the structural group dipole in Fig. 5b. Viewing

170   the dipole in Figs. 5c and 5d together with Fig 7b, one sees that most of the Si atoms and all of

171   the O atoms undergo small shifts and some small exchanges. The lengths of the shuffle vectors

172   range from 0.01 *nm* to 0.06 *nm*.

173   The end members of the dipole undergo much larger shuffles. Figure 8a shows just the end

174   arrangement of the dipole. In order to satisfy the mirror symmetry, these Si and Al toms must

175   switch positions in the dipole. The specific view of a portion of the SDC along the dipole axis in

176   Fig. 8b shows that these shuffles are large (0.26 to 0.46 nm), roughly an order of magnitude

177   larger than the other shuffles. These are so large that that it may be energetically favorable for

178   the Si and Al atoms to shuffle to the wrong type of site as in Fig. 8c, creating anti-site defects

179   and disorder. These would have much smaller shuffles, 0.06 *nm*, of the order of the smaller shifts

180   of oxygen and the Si atoms other than the end members. The resulting structure would be a

181   pseudo-twin as depicted in Fig. 9. The shuffles nominally parallel to the interface are more

182   probable. They are shorter, which means that their self-energy is smaller. Also, they are less

183   likely to produce local, non-linear displacements normal to the interface, implying a smaller

184   contribution to the activation energy for disconnection motion.

185   In general, if shuffles are incomplete, there could be two levels of pseudo-twin formation.

186   First, no shuffles could accompany disconnection motion, with all later occurring by thermal

187   relaxation. Second, the smaller shift-type shuffles could accompany disconnection motion, with

188   only the exchange-type shuffles then occurring by thermal relaxation. Both are possible, since

189   the atomistic simulation of the relaxation of an ideal albite twin by the even smaller local

190   nonlinear displacements near the boundary also required thermal activation (Li and Knowles,

191   2013).

192   **2.3. The Ideal Bicrystal**

193   There are several procedures to determine disconnection characteristics. The traditional

194   scheme is to use the coherent CDP to determine **b** and *h*, and the CDC to find all displacements

195   **u**. In the formation of the ideal bicrystal (the final reference space) from the CDC, these

196   displacements are separated into **b**, **s**, and **p** vectors. This method best reflects the underlying

197   symmetry and is preferable for simple crystals. This type of CDC is illustrated in Fig. A1b.

198   Alternatively, one can use the SDC shifted by **b** and **p**, leaving only the SDC for the step

199   portion of the dislocation (Hirth et al., 2016).   Such a SDC is illustrated for the case where **p** is

200   zero in Fig. A1c. Only shuffles are present in this reduced SDC, as given by Eq. (3). In the e-cell

REVISION 2

201   of the SDC, the rotation of the atomic dipole suffices to yield all shuffles. Thus, as shown here,

202   the latter method simplifies the determination of shuffles when the crystal structure is complex.

203   In progressing from the CDC to the SDC to the ideal bicrystal, there is a continued reduction in

204   symmetry.

205   The ideal Bilby bicrystal is perfect on either side of the interface (Hirth et al., 2013). This is

206   the space that is used in conjunction with ordinary Burgers circuits. As illustrated in Figure A1a,

207   a dividing surface in the CDC is located midway between the last plane transformed and the next

208   untransformed plane (Pond et al., 2016). Hence, it is displaced from the coherent interface in the

209   CDC by $d/2$, where d is the interplanar spacing (the twin symmetry plane remains the coherent

210   plane). Matrix atoms are removed below the dividing surface and twin planes are removed

211   above the dividing surface, creating the Bilby bicrystal, which also has an interface displaced

212   from atomic planes by $d/2$. This interface corresponds to the thermodynamic Gibbs interface. In

213   this reference bicrystal, one could construct circuits around a defect to determine **b**. However,

214   the CDC would still be needed to determine shuffles.

215   The real bicrystal, another representation, would have additional strains, but these would be

216   localized to the near-interface region. These nonlinear strains are not considered here. They

217   could be found in an atomistic simulation or possibly by atomic resolution HRTEM.

218   **3. Imperfect defects**

219   Imperfect defects are most conveniently depicted in the CDC. For such defects, the vectors

220   analogous to $\mathbf{t}_\lambda$ do not connect the origin to a lattice site in λ: hence, they are designated as

221    $\mathbf{q}(\lambda)$. Consequently, there is a stacking fault on one side of the defect. Eq. (1) is modified to

222                                    $$\mathbf{b} = \mathbf{q}(\lambda) - \mathbf{t}(\mu) \tag{4}$$

REVISION 2

223   One simple example is a 1/2<112> partial in a face centered cubic (*fcc*) structure. Another is the

224   defect observed in Al when a 1/3 <111> disconnection at a twin boundary dissociated into a

225   1/9<111> partial and a 2/9<111> partial (Pond, 1989). Such imperfect defects do not form unless

226   the fault associated with $\mathbf{q}_\lambda$ is low in energy, which usually requires that $\mathbf{q}_\lambda$ is rational. For

227   example, the intrinsic fault associated with a 1/6<112> partial in fcc is rational, has local

228   symmetry and is associated with low stacking fault energy. Similar defects are found in layer

229   structures such as graphite and mica, Amelinckx (1964).   Another special type relates to CDCs

230   with simple dipoles or multipoles at cell sites. The structural group dipole in Fig. 6a is of this

231   type. This CDC can be envisioned as two interpenetrating, simple, triclinic, structural group

232   complexes, A (red) and B (gray). A possible partial is one with **b** connecting an A site to a B

233   site. Similarly, a shuffle vector could connect A and B sites. These are more likely when h is $2h_0$

234   or more, since the local strains accompanying shuffles decrease with increasing h. Shuffles of

235   this type have been observed in a simulation of hcp $(11\overline{2}0)$ twinning in Zr (Khater et al., 2013).

236   Partials of this type also have been associated with disconnections of a synchroshear type in

237   alumina (Krönberg, 1957), olivine-spinel transformations (Poirier, 1981), and in Laves phases

238   (Hazzledine and Pirouz, 1993). In most cases, the glide plane or twin plane has sufficient

239   symmetry that a given fault can be created either by glide (*e.g.,* by a 1/6<112> partial in *fcc*) or

240   by climb (*e.g., by a* 1/3<111> partial in *fcc*).

241   **4. Other defects**

242   Several other defects including disclinations (Barrett and El Khaderi, 2014), facets (Li et al.,

243   2010), interface junctions (Pond, 1989), and type II twins (Pond and Hirth, 2018), have been

244   described with the TM. By applying the concept of structural groups, one can describe these

245   defects in an identical manner to that presented here. In all cases, including the defects described

REVISION 2

246   in Sections 2 and 3, the kinetics of motion entail the addition of atoms at kinks or jogs on the

247   defect lines. Discussion of the details is beyond the scope of the present treatment. For

248   disconnections in either the phase transformation case or the twinning case, the activation energy

249   for defect motion has contributions from shuffle motions, not simply those associated with the

250   dislocation component.

251   **5. Discussion**

252   Much of the description here entails tractable methods for determining shuffles in

253   complex minerals. The simpler CDP suffices to define **b**, h, and the shear accompanying

254   twinning.   The complete description of a disconnection entails the shuffles (**s**) as well.

255   Understanding the shuffles is essential in determining the most likely disconnection for a given

256   twin and in modeling disconnection motion (twin growth). The basic concept, incorporated in

257   the TM, is that the most likely disconnection is that with the shortest set of shuffle vectors (Bilby

258   and Crocker, 1965; Christian and Mahajan, 1995). For albite, we see that the determination of

259   shuffle vectors is greatly simplified if one first removes the shuffles associated with the structural

260   groups (which removes effects associated with **b** and **p)**, and then uses the SDC to determine the

261   remaining shuffles. Our analysis also demonstrates the possibility (likelihood) of large steps with

262   many shuffles, based on the requirement for switching of atoms from Si and Al sites; the

263   application of these techniques for twinning in plagioclase solid solution phases could involve

264   similar steps related to switching between Ca-Na sites.

265   The major focus of the mechanistic applications of the TM has been on phase

266   transformations and twinning. There are other disconnection models and mechanisms with many

267   similarities. In particular we note the extensive work on grain boundary sliding (e.g., Han et al.,

268   2018; Rajabzadeh et al., 2014; Combe et al., 2016), a process that has been interpreted to be

REVISION 2

269 important for a number of geologic materials, including olivine (e.g., Hansen et al., 2011), calcite

270 (e.g., Austin et al., 2014), plagioclase (Miranda et al., 2016), and quartz (Cross et al., 2017). In

271 all of these applications, the reference lattices provide the basis for the application of the TM to

272 all disconnection models. While earlier work emphasized the importance of interface steps for

273 phase transformations (e.g., Howe and Smith, 1992), twinning (e.g., Hardouin and Duparc,

274 2017), and grain boundary sliding (e.g., Langdon, 2006), the formal description of the TM is not

275 trivial (Hirth et al., 2013; Han et al., 2018). Long-range fields are associated with the Burgers

276 vector for dislocation components or the Frank vector for disclination components. The motion

277 of the step component produces pure rotation related to disclination quadrupoles. Similarly, the

278 reference spaces of the TM describe spacing defects, line forces, and non-equilibrium structures.

279 The motion of the step component produces pure rotation related to disclination quadrupoles.

280 We emphasize that the shuffles found in the reference spaces of the TM are important in

281 describing the mechanism of disconnection motion, e.g., in twin growth. In atomistic simulations

282 of twin growth, it is important to determine the height and Burgers vector (or Frank vector) for

283 the most likely disconnection In this case, for a given growth rate the twin stress can be

284 predicted. In one example, only the TM accurately predicts the geometry of a type II twin

285 (Pond et al., 2018). Many researchers are employing disconnections and advancing new ideas,

286 mainly for simple structures. In all cases, the concept of structural groups would be a useful tool

287 for the extension of this body of work to complex minerals.

288 The topic of disconnections is a burgeoning field. We anticipate that there will be many

289 applications for minerals. We have given one example of twinning for low albite. The twin

290 methodology should be important in the computer simulation of deformation twin growth, and in

291 modeling dislocation-twin intersections. The same TM methodology can be applied to order-

REVISION 2

292   disorder transformations, phase changes, slip, defect-boundary interactions, and boundary details

293   such as facets. The TM concepts described here can serve as a template to analyze these

294   processes as well. What we have emphasized here is that the analysis of structural aspects of

295   disconnections, most importantly shuffling, can be simplified by treating unit cells of complex

296   structures comprised of structural groups.

297   **6. Implications**

298   The model presented here describes the mechanism for deformation twinning and applies as

299   well to shear-type transformations and grain boundary deformation. We chose to illustrate the

300   model for twinning in albite owing to its potential application for constraining the rheological

301   properties of the crust at conditions near the brittle-plastic transition, where plagioclase is a

302   major constituent of common rock types. While deformation twins in plagioclase are often

303   described from microstructural analyses in crustal rocks, the interpretation of the stress states at

304   which they form has not advanced – partly owing to difficulties in quantifying constitutive laws.

305   The concept of structural groups makes analysis of the twinning transformation process easier in

306   complex minerals and explicitly predicts the interface structure of the deformation

307   twins. Twinning is particularly important at lower temperatures, where creep by diffusional

308   relaxation is limited and large stress concentrations arise at triple points and near grain

309   boundaries. At these conditions dislocation slip in plagioclase becomes limited, partly because

310   of the large Burgers vectors. Twinning then becomes a possible mechanism to satisfy the von

311   Mises requirement and to accommodate stress concentrations. Recent advances in

312   microscopy (e.g., high-angular resolution electron backscatter diffraction, Wallis et al.,

313   2016) presage new analyses of twinning in feldspars (as well as other minerals) that could be

314   used to investigate stress states at these conditions, in addition to the role of crystal plasticity

315   during semi-brittle flow and fracture near the base of the seismogenic zone, and in regions near

316   impacts.

317

318   Atomistic simulation of deformation is a burgeoning field. For twinning simulations, the TM

319   analysis is useful in providing the likely twinning disconnection and the proper boundary

320   conditions. The shear and the shuffles provide a basis for analyzing the activation energy

321   (including the stress dependence) for twin growth, important in developing constitutive relations

322   for deformation, which in turn provide input for analyzing the microstructure of polycrystals.

323   This is important because twins created in the laboratory can form at rates up to eight orders of

324   magnitude faster and have twin sizes two or three orders of magnitude smaller than those formed

325   naturally. Thus, if the interface structures observed in high-resolution electron microcopy are the

326   same for both laboratory and natural structures, then constitutive relations for deformation

327   (determined in the laboratory) should also apply to the natural twins. Knowledge of the

328   constitutive relations enables one to know the critical stress and temperature for the twinning-slip

329   transition. Disconnection concepts apply directly to grain boundary sliding and twinning and

330   would also be essential in developing constitutive relations for these processes.

331

332   **7. Summary**

333   Elements of the Topological Model for disconnections, dislocations and interfaces are

334   presented. For crystals with many atoms in the unit cell, some properties can be deduced from

335   spaces of structural groups. Each structural group is an atomic motif referred to a position in the

REVISION 2

336   crystal structure (unit cell). The cells of structural groups yield the proper crystal lattice. Paired

337   crystal lattices comprise the coherent dichromatic pattern (CDP) and paired crystal structures

338   comprise the lower symmetry, coherent dichromatic complex (CDC). Burgers vectors of

339   transformation or twinning disconnections are mapped directly in the CDP. The shuffles that

340   accompany transformation or twinning are determined from the CDC or its geometric variants,

341   i.e. SDC and RDC. As demonstrated for twinning in albite, the shuffles are related to the rotation

342   of a single structural group dipole, providing a simple method for their determination.

343   **Acknowledgments**

348

349

REVISION 2

References

351 Amelinckx, S. (1964) The direct observation of dislocations. Solid State Physics Suppl 6.

352 Anderson, P.M., Hirth, J.P., and Lothe J. (2017) Theory of dislocations, 3rd ed., 699 p.
353   Cambridge University Press, U.K.

354 Austin, N., Evans, B., Rybacki, E., and Dresen G. (2014) Strength evolution and the
355   development of crystallographic preferred orientation during deformation of two-phase
356   marble. Tectonophysics, 631, 14-28.

357 Barrett, C.D., and EI Khadiri, H. (2014) The roles of grain boundary dislocations and
358   disclinations in the nucleation of {10$\underline{1}$2} twinning. Acta Materialia 63, 1-15.

359 Bilby, B.A., and Crocker, A.G. (1965) The theory of the crystallography of deformation
360   twinning. Proceedings of the Royal Society (London), A288, 240-255.

361 Christian, J.W., and Mahajan, S. (1995) Deformation twinning. Progress in Materials Science,
362   39, 1-157.

363 Combe, N., Mompiou, F., and Legros, M. (2016) Disconnections kinks and competing modes in
364   shear-coupled grain boundary migration. Physical Review B, 93, 024109, 1-6.

365 Cross, A.J., Hirth G.,, and Prior, D.J., Effects of secondary phases on crystallographic preferred
366   orientations in mylonites, Geology, 45, 955-958.

367 Hahn T, Ed. (2014) International tables for crystallography. New York: Wiley.

368 Han, J., Thomas, S.L., and Srolovitz, D.J. (2018) Grain-boundary kinetics: A unified approach.
369   Progress in Materials Science, 98, 386-476.

370 Hardouin Duparc, O.B.M. (2017) A review of some elements for the history of mechanical
371   twinning centred on its German origins until Otto Mügge's K1 and K2 invariant plane
372   notation. Journal of Materials Science, 52, 4182-4196.

REVISION 2

373   Hansen, L.N., Zimmerman, M.E., and Kohlstedt, D.E. Grain boundary sliding in San Carlos

374   olivine: Flow law parameters and crystallographic-preferred orientation (2011), J. Geophys.

375   Res., 116.

376   Hazzledine, P.M. and Pirouz, P. (1993) Synchroshear transformations in Laves phases. Scripta

377   Metallurgica, 28, 1277-1282.

378   Hirth, J.P., and Pond R.C. (1996) Steps, dislocations and disconnections as defects relating to

379   structure and phase transformations. Acta Materialia, 44, 4749–4763.

380   Hirth, J.P., Wang J., and Tomé C.N. (2016) Disconnections and other defects associated with

381   twin interfaces. Progress in Materials Science 83, 417-471.

382   Hirth, J.P., Pond R.C., Hoagland R.G., Liu X.Y., and Wang J. (2013) Interface defects, reference

383   spaces and the Frank-Bilby equation. Progress in Materials Science, 58, 749–823.

384   Howe, J.M., and Smith D.A. (1992) Comparison between the invariant line and structural ledge

385   theories for predicting the habit plane, orientation relationship and interface boundary

386   structure of plate-shaped precipitates, Acta Metallurgica et Materialia, 40, 2343-2350.

387   Howe J.M., Dahmen U., and Gronsky R. (1987) Atomic Mechanisms of precipitate plate growth,

388   Philosophical Magazine, A56, 31-61.

389   Howe, J.M., Pond, R.C., and Hirth, J.P. (2009) The role of disconnections in phase

390   transformations. Progress in Materials Science, 54, 792–838.

391   Khater, H.A., Serra, A., and Pond R.C. (2013) Atomic shearing and shuffling accompanying the

392   motion of twinning disconnections in zirconium. Philosophical Magazine, 93, 1279-1298.

393   Krönberg, M.L. (1957) Plastic deformation of single crystals of sapphire: basal slip and

394   twinning. Acta Metallurgica, 5,507-524.

REVISION 2

395 Langdon, T.G. (2006) Grain boundary sliding revisited. Journal of Materials Science 46, 597-
396   609.

397 Li, B., and Knowles, K.M. (2013) Molecular dynamics simulation of albite twinning and
398   pericline twinning in low albite. Model Simul Mater Sci Eng 21:05501.

399 Li, Y.J., Chen, Y.J., Walmsley, J.C., Mathinsen, R.H., Dumoulin, S., and Roven, H.J. (2010)
400   Faceted interfacial structure of {1011} twins in Ti formed during equal channel angular
401   pressing. Scripta Materialia 62, 443-446.

402 Medlin, D.L., and Yang, N.Y.C. (2011) Interfacial step structure at a (0001) basal twin in
403   Bi_2Te_3. Journal of Electronic Materials, 41, 1456-1454.

404 Miranda, E.A., Hirth, G, and B.E. John, B.E. (2016) Microstructural evidence for the transition
405   from dislocation creep to dislocation-accommodated grain boundary sliding in naturally
406   deformed plagioclase. J. Structural Geology, 92, 30-45.

407 Poirier J.P. (1981) On the kinetics of olivine-spinel transition. Physics of the Earth and Planetary
408   Interior, 26, 179-187.

409 Pond, R.C. (1989) Line defects in interfaces. In: F.R.N.Nabarro, Ed. Dislocations in solids, vol.8,
410   p. 5-66. Elsevier, Amsterdam.

411 Pond, R.C., and Hirth, J.P. (1994) Defects at surfaces and interfaces. Solid State Physics 47, 287-
412   365.

413 Pond, R.C., and Hirth, J.P. (2018) Topological model of type II deformation twinning. Acta
414   Materialia 151, 229-242.

415 Pond, R.C., and Vlachavas, D.S. (1983) Bicrystallography. Proceedings of the Royal Society
416   (London), 386A, 95-143.

REVISION 2

417   Pond, R.C., Hirth, J.P., Serra A., and Bacon D.J. (2016) Atomic displacements accompanying

418   deformation twinning: shears and shuffles. Materials Research Letters, 5, 541-544.

419   Pond R.C., Ma X., Chai Y.W., and Hirth J.P. Topological modelling of martensitic

420   transformations. In: F.R.N. Nabarro and J.P. Hirth, Eds. Dislocations in solids, vol.13, p.

421   225-262, Elsevier, Amsterdam.

422   Rajabzadeh, A., Mompiou, F., Lartigue-Korinek, S., Combe, N., Legros, M., and Molodov, D.A.

423   (2014) The role of disconnections in deformation-coupled grain boundary migration. Acta

424   Materialia, 77, 223-235.

425   Ribbe, P.H. (1974) In: Feldspar Minerals, Vol.1. Crystal structure and physical properties.

426   Springer-Verlag, p. 1-19.

427   Serra, A., Pond, R.C., and Bacon, D.J. (1991) Computer-simulation of the structure and mobility

428   of twinning dislocations. Acta Metallurgica et Materialia, 39, 1469-1480.

429   Wallis, D., Hansen, L.N., Britton, T.B., and Wilkinson, A.J., (2016) Geometrically necessary

430   dislocation densities in olivine obtained using high-angular resolution electron backscatter

431   diffraction, Ultramicroscopy, 168, 34–45.

432   Wenk, H-R, Bulakh A (2016) Minerals: their constitution and origin. Cambridge, Cambridge

433   University Press.

434

435   **Figure Captions**

436   Fig. 1. Conventional unit cell of low albite.

437   Fig. 2. Conventional crystal lattice in black. Alternate (smaller) lattice in red.

REVISION 2

438   Fig. 3. Coherent dichromatic pattern (CDP) for an [001] (010) twin in albite. Translation

439   vectors and **b** shown for an $h = h_0$ disconnection. (a). Projection along $[00\bar{1}]$. (b). Projection

440   along the normal to $[0\bar{1}0]$.

441   Fig. 4.   Schematic of disconnection. (a) Two free surfaces, with translation vectors and h

442   labelled, are joined to create coherent terraces bounding a disconnection (b), with **b** shown

443   for $h = h_\lambda$.

444   Fig. 5. (a). Unit cell of structural group dipoles. (b). Atomic motif of one structural group

445   dipole. (c). Projection of Fig. (b) normal to **b**, or [001]. (d). Projection of Fig. (b) normal to

446   b^*, *i.e.,* normal to $(001)^0$.

447   Fig. 6. CDC for structural groups viewed along a and normal to the (010) plane. Rotation of

448   the structural group dipole in the CDC also shown.

449   Fig. 7. (a). Repeat unit of two $(001)^0$ planes viewed along $[\bar{1}0\bar{1}]^0$. Solid line will become

450   the twin symmetry plane and the dashed line will become the twin interface. Matrix part of

451   e-cell is enclosed in red. (b). Structure of Fig. (7a) is sheared by **b** above the twin boundary,

452   but no shuffles are imposed. In Fig. 7(b), shuffles are added to the matrix part of the e-cell

453   of Fig. 7(a). The extension of the e-cell to encompass the entire region above the twin plane

454   creates the CDC. Fig. 7(c) is the matrix part of the e-cell in the SDC, with **b** subtracted from

455   Fig. 7(b)**.**

456   Fig 8. (a). Atoms at the ends of the structural group dipoles in the e-cell in Fig 5(b) viewed

457   along the dipole axis. The atoms must shuffle as shown the satisfy mirror symmetry. (b).

458   Specific shuffles in a portion of the SDC. c. Shorter shuffles, creating anti-site defects.

459   Fig. 9. Pseudo-twin, with the anti-site defects of Fig. 8 unrelaxed.

REVISION 2

460   Fig A1. (a). Ideal Bilby bicrystal for a (103) twin in a simple cubic structure. The position

461   of the interface is shown as solid line. (b). Corresponding CDP/CDC for a $h = 3h_0$

462   disconnection is depicted, along with associated **b** and **s** vectors. Position of dividing

463   surface shown as solid line, resultant twin symmetry plane by dashed line. (c). Shifted SDC

464   with the μ structure shifted by **b** relative to λ. The **s** vectors are the same as those in Fig.

465   (b).

466   Fig. A2. (a) Schematic of disconnection traversing the twin. The disconnection with

467    $h = 3\,h_0$ moves to the right and converts region C from matrix A to twin C, growing twin

468   D. In the wake of the defect. the matrix region B is displaced by **b**. In region C the matrix

469   is displaced by a combination of shear by **b** and shuffles **s**.

470

Appendix A. The TM methodology for a twin in a simple cubic lattice

472   Figure A1a illustrates the methodology of the TM for a (103) twin in a simple cubic, $\Sigma 5$

473   crystal. The plane of twin symmetry is shown as a solid line. The CDP is shown in Fig. A1b.

474   Inspection of the CDP reveals that the probable disconnection has $h = 3h_0$ with **b** as shown.

475   The Burgers vector $when\ h = h_0$ has an elastic energ*y* $\propto b^2$ that is four times as large. The

476   Burgers vector is smaller for $h = 2h_0$ but the shuffle vectors are large, so it would be difficult

477   to nucleate. For $h = 3h_0,$ both **b** and h are relatively small. For this example, the CDP and the

478   CDC coincide. The dividing surface, the solid line in Fig. A1b, is located midway between the

479   last twin plane transformed and the next untransformed matrix plane. It is displaced by $d/2$ from

480   the coherent interface in the CDC to the red position, where $d,$ here equal to h_0 is the interplanar

481   spacing (the twin symmetry plane, dashed line, remains the coherent plane). Matrix atoms are

REVISION 2

482   removed below the dividing surface and twin planes are removed above the dividing surface,

483   creating the Bilby bicrystal (Hirth et al., 2013), which also has an interface displaced from

484   atomic planes by d/2. This interface corresponds to the thermodynamic Gibbs interface.

485   The former matrix atoms must undergo added displacements so that the crystal structure is

486   correctly that of the twin.   This is accomplished by the shuffles. Shuffles are local atom

487   rearrangements that produce no plastic strain but which complete a transformation. In the CDC,

488   the displacements are $\mathbf{u}^0(\lambda)$ and $\mathbf{u}^0(\mu)$. The shuffle vectors $\mathbf{s}_1$ and $\mathbf{s}_2$ (which quantify the

489   displacements associated with the rearrangement of atoms) for the (103) twin are depicted in

490   Figs. A1b and A1c. These vectors are of the exchange type. As noted in Section 2.2, the shuffles

491   are related to the displacements in the CDC by $\mathbf{s} = \mathbf{u}^0(\lambda) - \mathbf{b}.$ Figure A1c demonstrates the

492   SDC for the (103) twin. In the SDC, the displacements are $\mathbf{u}(\lambda)$ and $\mathbf{u}(\mu)$, and the shuffles are

493   given by $\mathbf{s} = \mathrm{u}(\lambda)$. The matrix above the dividing surface is already sheared by $\mathbf{b}$ in this

494   diagram**.**

495   Physically, if a disconnection moves along the interface, the entire matrix above the interface

496   is shifted by the Burgers vector. This is represented in a schematic view of the real crystal in

497   Fig. A2. Above the red line in Fig. A1b, that is all that happens. Between the dark and red lines,

498   the matrix has been converted to the twin. Thus, the matrix atoms are displaced to the left by $\mathbf{b}$

499   in region B while atoms in region A are not displaced.   Atoms are also displaced in region C.

500   However, this leaves the structure in this little region in incorrect positions.   Shuffles are

501   required in region C to complete the twinning transformation. Hence, disconnection motion

502   requires both shear and shuffles, creating a perfect twin increment in its wake.

503   To connect to the mineral applications, Fig. A1 could represent reference spaces for

504   structural groups in a complex cubic crystal.
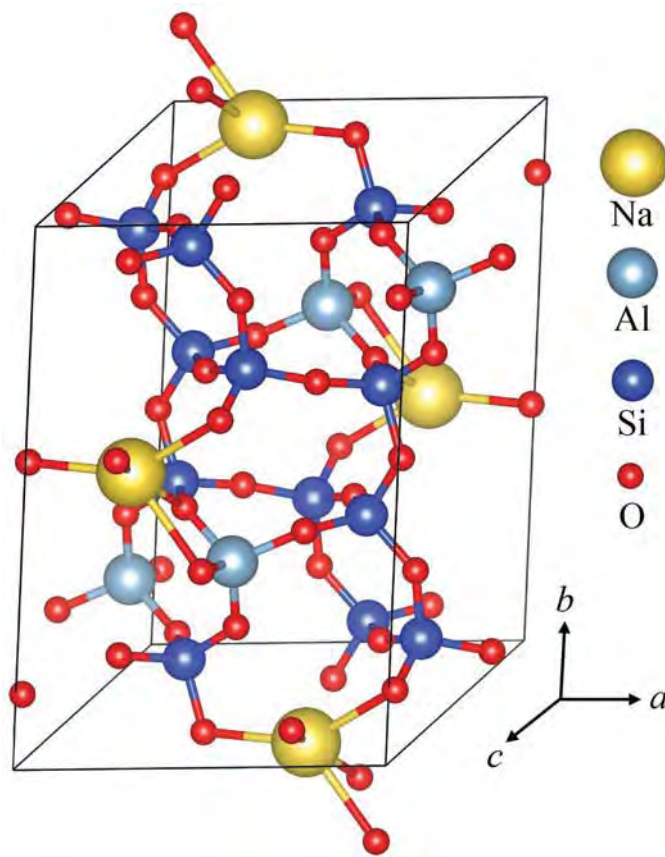
REVISION 2

505

506

Figure 1

Fig. 1. Conventional unit cell of low albite.
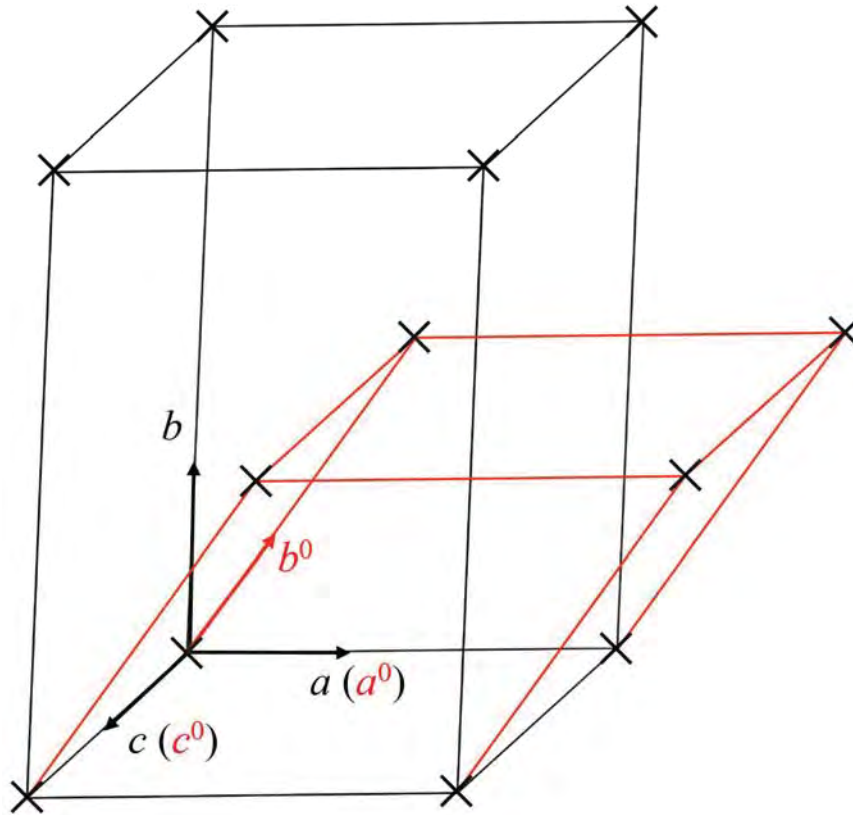
Figure 2

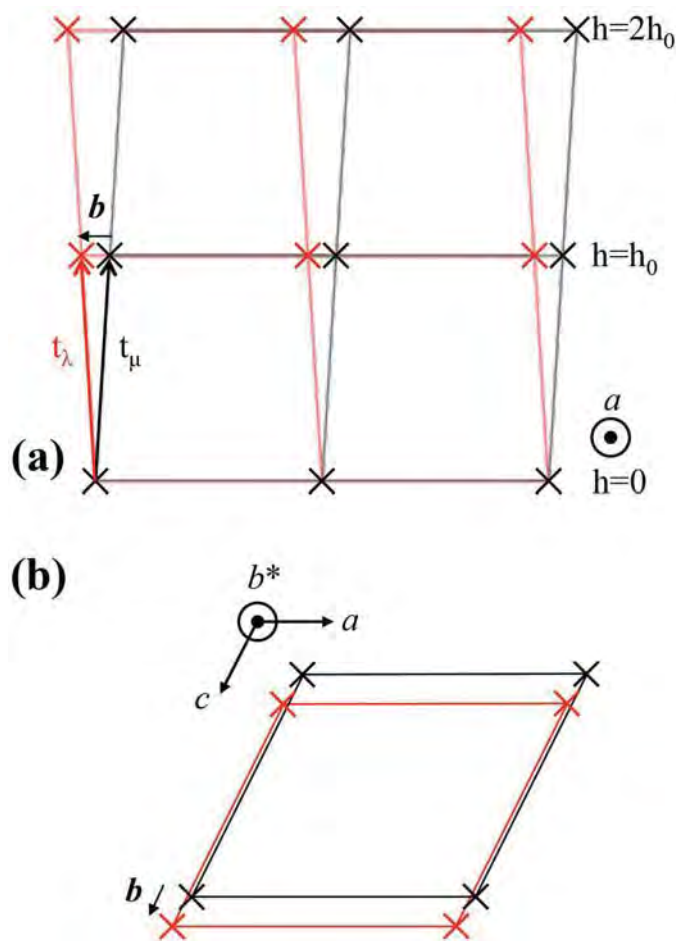Fig. 2. Conventional crystal lattice in black. Alternate (smaller) lattice in red.

Figure 3

Fig. 3. Coherent dichromatic pattern (CDP) for an [001] (010) twin in albite. Translation vectors and **b** shown for an $h = h_0$ disconnection. (a). Projection along $[00\bar{1}]$. (b). Projection along the normal to $[0\bar{1}0]$.
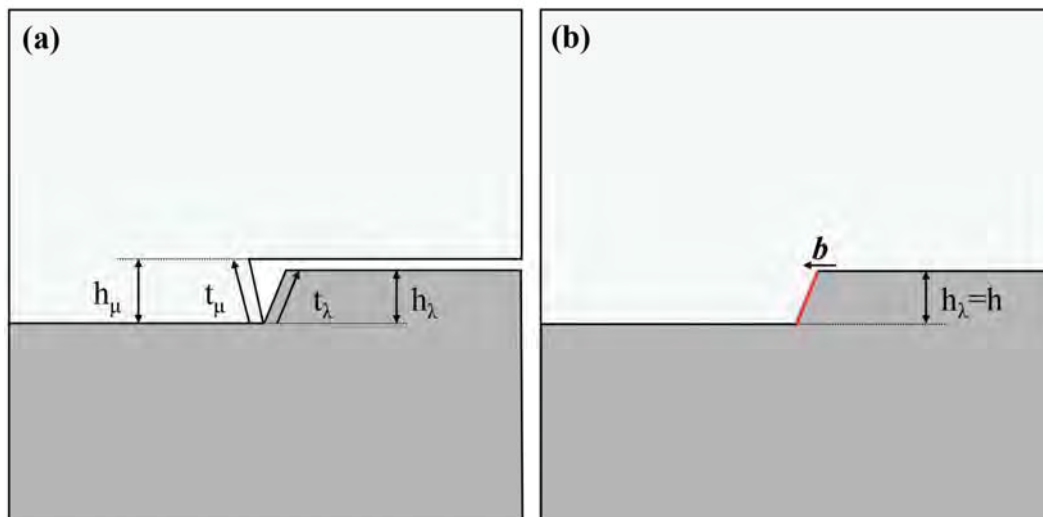
3

Figure 4

Fig. 4.   Schematic of disconnection. (a) Two free surfaces, with translation vectors and h labelled, are joined to create coherent terraces bounding a disconnection (b), with **b** shown for $h = h_\lambda$.

4
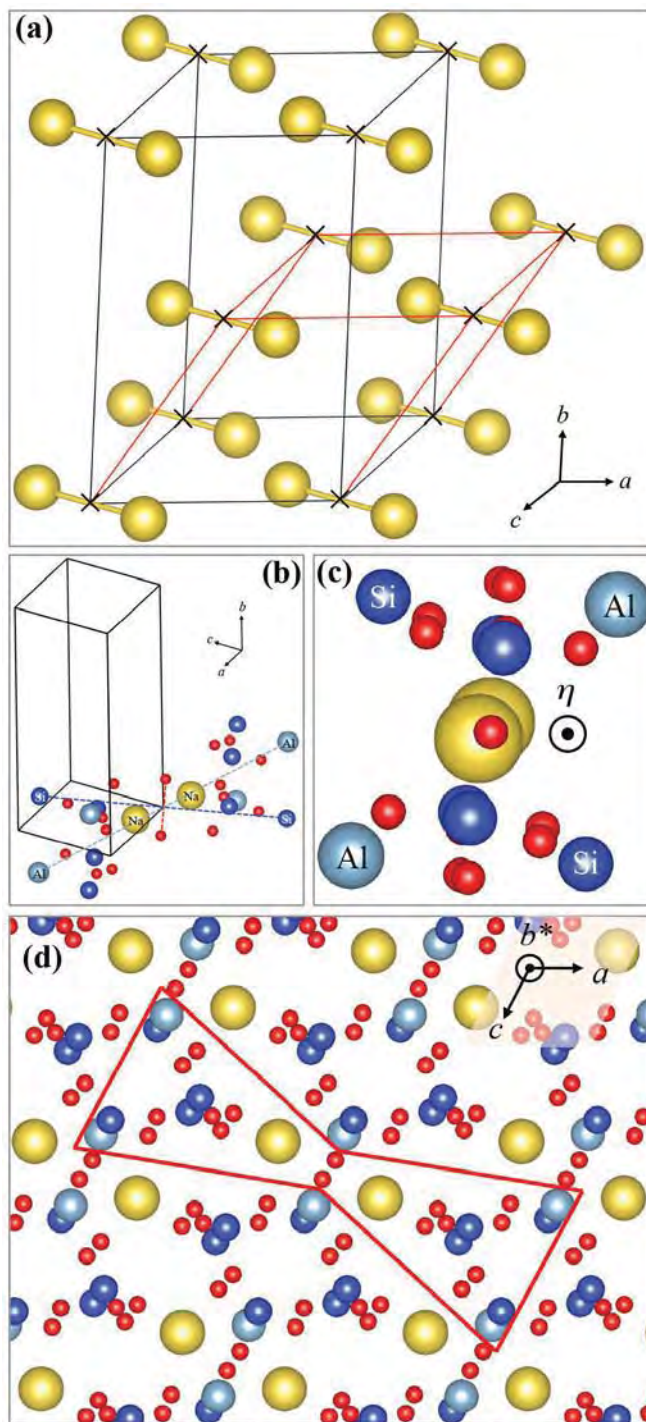
Figure 5

Fig. 5. (a). Unit cell of structural group dipoles. (b). Atomic motif of one structural group

dipole. (c). Projection of Fig. (b) normal to **b**, or [001]. (d). Projection of Fig. (b) normal to
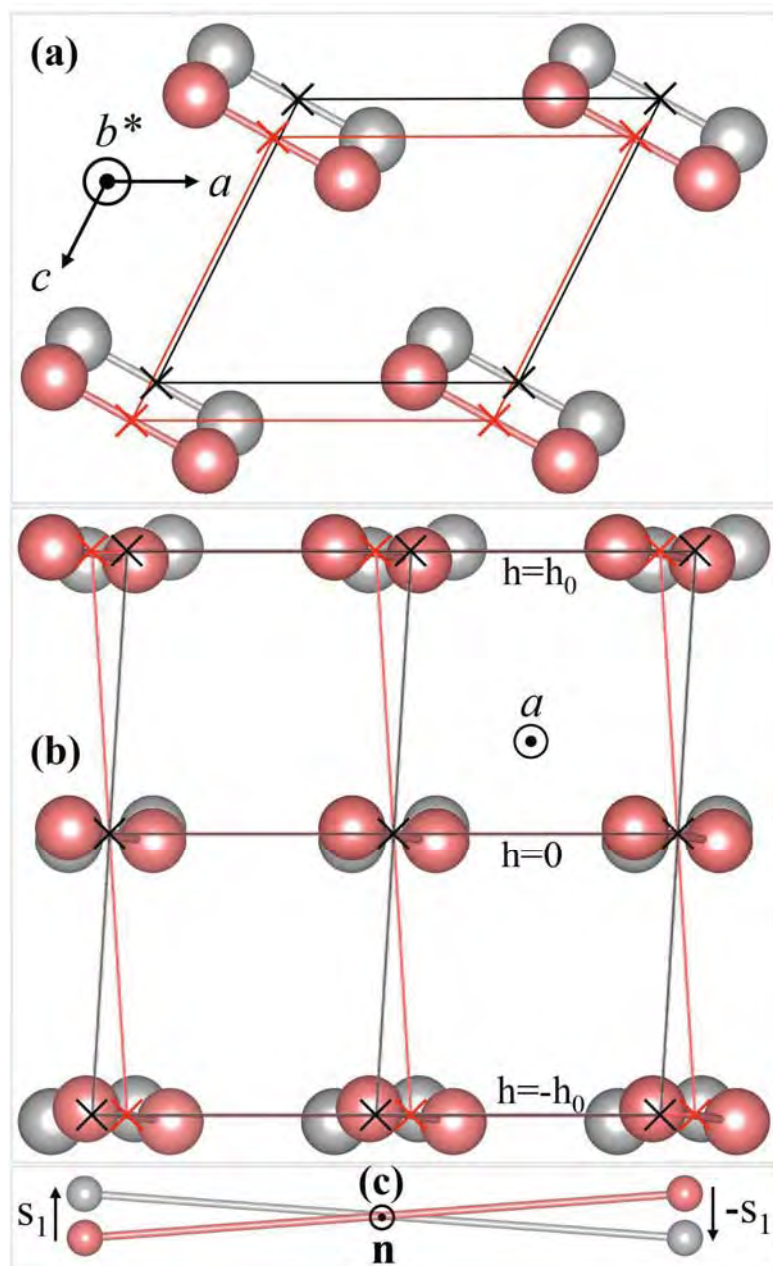
b^*, *i.e.,* normal to $(001)^0$.

Figure 6

Fig. 6. CDC for structural units viewed along a and normal to the (010) plane. Rotation of the structural unit dipole in the CDC also shown.
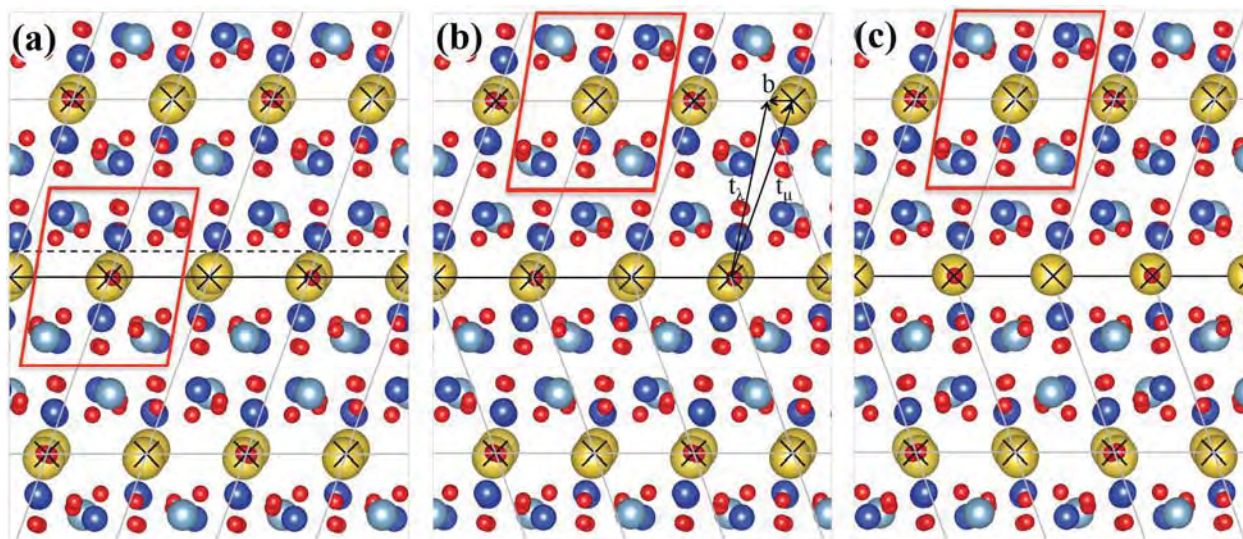
6

Figure 7

Fig. 7. (a). Repeat unit of two $(001)^0$ planes viewed along $[\bar{1}0\bar{1}]^0$. Solid line will become the twin symmetry plane and the dashed line will become the twin interface. Matrix part of e-cell is enclosed in red. (b). Structure of Fig. (7a) is sheared by **b** above the twin boundary, but no shuffles are imposed. In Fig. 7(b), shuffles are added to the matrix part of the e-cell of Fig. 7(a). The extension of the e-cell to encompass the entire region above the twin plane creates the CDC. Fig. 7(c) is the matrix part of the e-cell in the SDC, with **b** subtracted from Fig. 7(b).
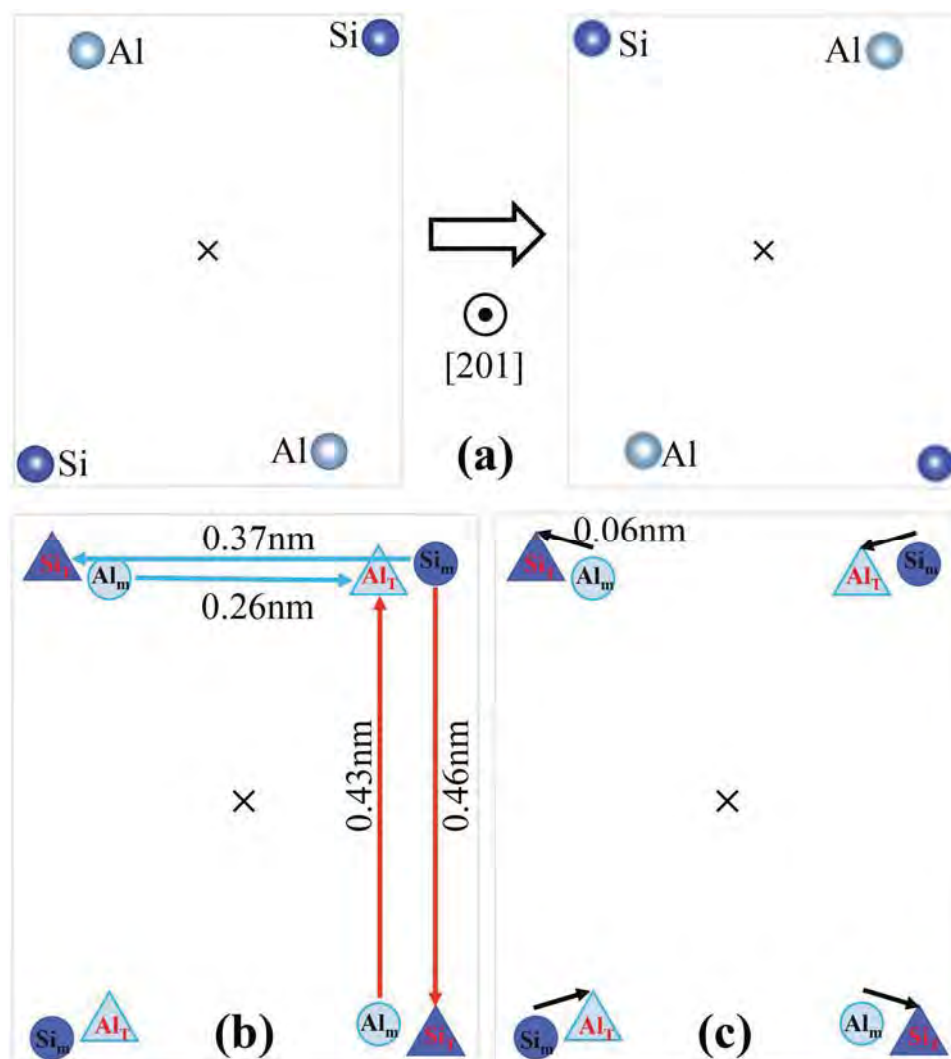
7

Figure 8

Fig 8. (a). Atoms at the ends of the structural group dipoles in the e-cell in Fig 5(b) viewed along the dipole axis. The atoms must shuffle as shown the satisfy mirror symmetry. (b). Specific shuffles in a portion of the SDC. c. Shorter shuffles, creating anti-site defects.
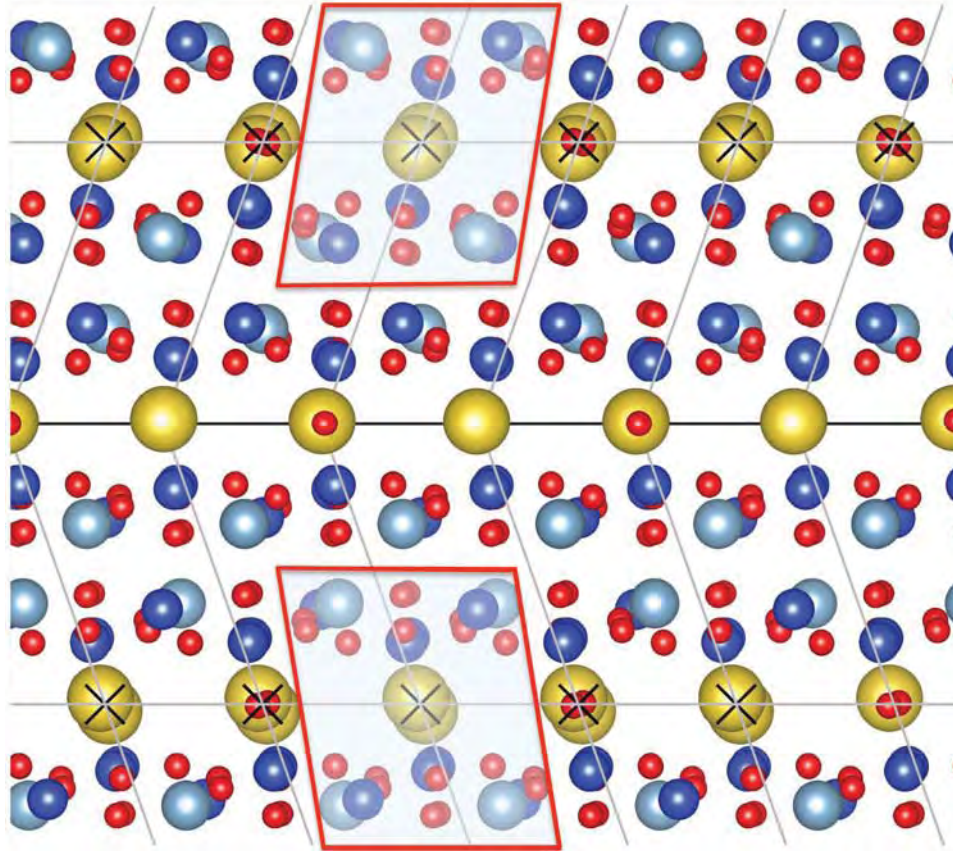
Figure 9

Fig. 9. Pseudo-twin, with the anti-site defects of Fig. 8 unrelaxed.